Off-energy operation for the Extremely Brilliant Source at the European Synchrotron Radiation Facility

L. Valle, T. Brochard, N. Carmignani, L. R. Carver, J. Chavanne, F. Ewald, G. Le Bec, S. M. Liuzzo, T. Perron, J. Reyes-Herrera, P. Raimondi, K. Scheidt, R. Versteegen, J. Wade, and S. White

European Synchrotron Radiation Facility-71, avenue des Martyrs, 38043 Grenoble, France

(Received 27 October 2023; accepted 25 April 2024; published 28 May 2024)

The European Synchrotron Radiation Facility Extremely Brilliant Source (ESRF-EBS) is the first fourth generation 6 GeV storage ring (SR) light source making use of the hybrid multibend achromat lattice, reaching a natural horizontal emittance of 140 pm rad. Further, reducing the horizontal emittance would provide a more brilliant and a higher quality photon source for the EBS users. One way of achieving this is to operate the SR off-energy. The first approach reduces the electron beam energy by −1%, which gives a 121 pm rad natural horizontal emittance. To fulfill operation requirements, the full ring had to be rematched, including both the quadrupoles and the sextupoles in the linear optics correction. The off-energy settings are then tested in the SR in terms of lifetime, injection efficiency, and operability.

DOI: 10.1103/PhysRevAccelBeams.27.051601

I. INTRODUCTION

The European Synchrotron Radiation Facility (ESRF) is one of the first fourth generation storage ring (SR) light sources [1,2]. Its upgrade from a double bend achromat (DBA) to the Extremely Brilliant Source (EBS) reduced the 6 GeV SR natural horizontal emittance from 4000 to 140 pm rad [3–5]. The new storage ring delivers a higher quality photon beam: a factor 30 gain in the hard x-ray brilliance and spatial coherence was demonstrated with EBS since August 2020, compared to its previous SR optics. The ESRF-EBS lattice is based on the hybrid multibend achromat (HMBA) scheme [6]. The Twiss functions, dispersion, and EBS layout are displayed in Fig. 1. The notations use the standard s for the longitudinal position $(x, x' = \frac{dx}{ds}, y, y' = \frac{dy}{ds})$ transverse plane coordinates. Two dispersion bumps, under which are located the sextupoles, are created by a total of four longitudinal-gradient dipoles, each composed of five permanent magnet modules. The nonlinear impact of the sextupoles is compensated by a $-I$ transformation, ensuring high beam lifetime and large dynamic aperture [7,8]. High gradient quadrupoles and dipole-quadrupole magnets (DQ) focus the electron beam, maintaining a low emittance.

In a dispersion-free zone, the electron beam size and divergence are entirely defined by its emittances and the β-functions [9]. Under this condition, higher brightness can be obtained by approaching the optimum β-functions and lowering the beam emittance [10]. Currently, two beam dynamics areas focusing on the improvement of the ESRF-EBS source characteristics are being studied. The first locally maintains a low β_y-function at the center of an in-vacuum insertion device allowing its operation with a lower gap. This optics adaptation is under experimental tests for an expected 40% increase in hard x-ray brilliance [11,12]. The second (subject of this paper) operates the SR off-energy to reduce its natural horizontal emittance. In this case, the electron beam goes off axis in high-gradient quadrupoles experiencing extra dipolar fields that increase the effect of radiation damping [13]; this damping effect is often obtained with the inclusion of reverse bending magnets in the linear design [14–16].

To change the beam energy, the rf frequency is varied around the synchronous condition defining a nonzero energy deviation δ according to [17]:

$$\delta = \frac{\Delta p}{p} = -\frac{1}{\alpha_C}\frac{\Delta f}{f}, \tag{1}$$

with p the electron momentum, f the rf frequency, Δf the frequency shift, and α_C the momentum compaction factor, under the assumption that it varies slowly with momentum. This scheme is widely used in colliders to increase their luminosity [18–20] and is successfully implemented in the ESRF injector booster: with an achieved 30% reduction in the booster emittance (from 120 to 85 nm rad) for higher injection efficiency into the EBS SR [21,22]. However, going off axis in the high-gradient magnets and sextupoles

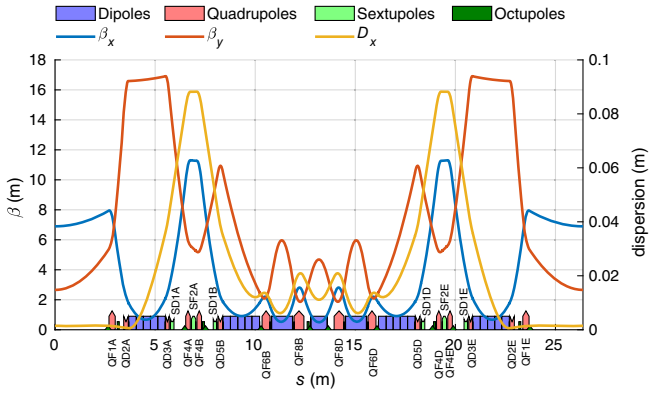

FIG. 1. Twiss functions of the standard hybrid multibend achromat (HMBA) cell of the ESRF-EBS storage ring lattice.

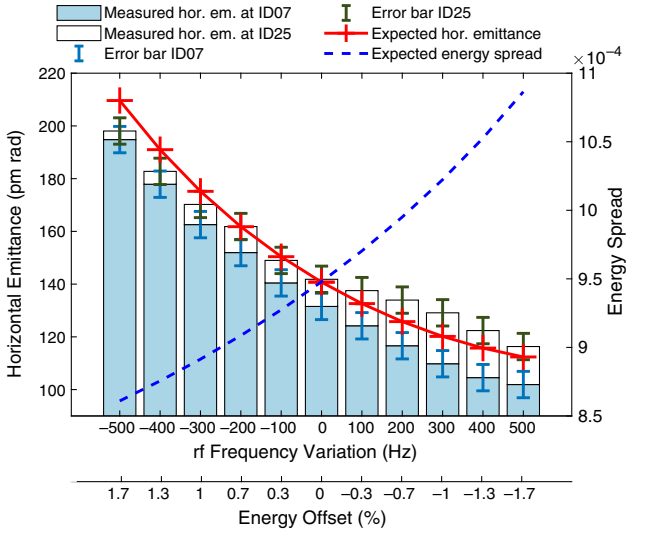

FIG. 2. Simulated and measured variations of the equilibrium horizontal emittance and expected energy spread with the rf frequency shift and corresponding energy offset ($\alpha_c = 8.62 \times 10^{-5}$). The emittance is measured at two pinholes located at the beginning of the cells 07 and 25 of the ESRF-EBS storage ring.

generates large distortions to linear optics. For instance, the optics variations introduced by a -1% change in the beam energy is, on average for the operational EBS lattice, $(\frac{\beta_{-1\%}-\beta_0}{\beta_0}) = (8.4\%, 3.7\%)$ and the dispersion variation 1.49 mm, both of which degrade the dynamic aperture (DA), the beam lifetime (LT), the injection efficiency (IE), and alter the photon sources parameters. After successful commissioning of synchrotron light sources, linear optics adaptation is common in selected straight sections to accommodate the end users, without degrading the overall performances and requirements for the system. Examples of such adaptations are available in [3,23–25].

In this paper, we present modified EBS optics (over the whole SR), matched to limit the performance degradation of the off-energy operation. These off-energy optics guarantee User Service Mode (USM) beam lifetime and injection efficiency very similar to the on-energy optics. In Sec. II, we will use a combination of approximated simulations, brilliance calculations, and experimental tests to define the best compromise for the off-energy operation setpoint ($\delta = -1\%$). The optics matching of the off-energy lattice including operational constraints (chromaticity, LT, and DA) is discussed in Sec. III. The on- and off-energy optics are then compared with tracking simulations of DA and LT and brilliance and spatial coherence for two typical EBS undulators. In Sec. IV, the details of the experimental validations of the off-energy operation are presented, which will include linear optics correction, Touschek lifetime optimization, and injection efficiency tuning.

II. ESTIMATED IMPACT ON SOURCE CHARACTERISTICS

The emittance reduction was first experimentally observed on the ESRF-EBS storage ring by simply varying the rf frequency without tunes, orbit, and optics corrections. Figure 2 compares the measured and simulated variations of the horizontal emittance and the expected energy spread in steps of 100 Hz between -500 and 500 Hz frequency shift range. The emittance measurement was corrected following the simulated variation of the β-functions and dispersion with the rf frequency. Simulations were conducted with Accelerator Toolbox (AT) [26,27]. A 22% reduction in the equilibrium horizontal emittance and an increase of 15% the energy spread were observed for approximately 1.7% reduction in the electron beam energy. The reduction of horizontal emittance should provide a higher brilliance and coherent fraction of the photon beam emitted by the insertion devices (ID). Nonetheless, the expected maximum brilliance per photon energy for lattices with both lower energy and lower emittance is not trivial.

In order to assess the potential brilliance gain, several 32-fold periodic ESRF-EBS HMBA rings were generated for different energy deviations down to -3.3%. Each cell linear optics were rematched to be as similar to the on-energy standard cell HMBA lattice as possible (see Fig. 1): conservation of the $-I$ transformation, the betatron tunes, and Twiss functions at the middle of the straight section for fair comparison. Matching and optics analysis were conducted using AT, and the characteristics of these lattices are detailed in Appendix A.

The obtained natural horizontal emittance and energy spread for each periodic lattice are shown in Fig. 3. The restoration of the HMBA Twiss functions and dispersion contributes to limit the emittance creation in the bending magnets and high-gradient quadrupoles in the off-energy lattices, while increasing the energy spread. Part of the discrepancy between the periodic and the uncorrected off-energy EBS natural emittances from Fig. 2 lays in the break

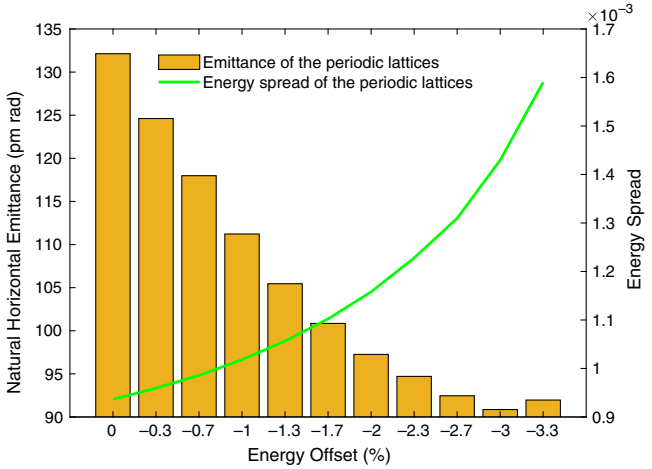

FIG. 3. Evolution of the natural horizontal emittance (bar) and the energy spread (green) of the periodic lattices with restored HMBA linear optics for different energy offsets.

of symmetry of the ESRF-EBS lattice (see Sec. III) partly due to the presence of dedicated photon sources [28].

Figure 4 shows the maximum relative brilliance of different photon beam energies of an in-air (U35) and an in-vacuum (CPMU18) insertion devices as a function of the rf frequency shifts and their respective periodic lattices. The reference brilliance is obtained with the on-energy optics at the nominal rf frequency. Calculations were done with the Synchrotron Radiation Workshop (SRW) software [29], assuming the same radiation energy or wavelength for both lattices as the first approach. This assumption required a larger gap for each undulator in the off-energy case to match the on-energy emitted photon energy, subsequently reducing the total radiated flux. An optimal compromise providing brilliance gain at low photon energies (10 and 20 keV) is found for an energy offset of −1.3% for which both insertion devices increase their brilliance by more than 5%. The range $[-1:-0.3]\%$ maximizes the gain of higher harmonics, rapidly limited by the effect of the higher energy spread, as displayed in Figs. 2 and 3 [30,31]. This effect is later observed on the two first harmonics, between −1.3% and −2.3% for both undulators. Additionally, the optics matching at large energy offsets proved to be challenging and approached the power supply limits of the dipole-quadrupole magnets. Therefore, the following study was conducted at an energy shift of −1% corresponding to a 300 Hz rf frequency shift.

III. OFF-ENERGY OPTICS

Off-energy linear optics need to be adjusted to recover performances as close as possible to USM conditions, within the ESRF-EBS power supply limits. For simplicity, the on-energy HMBA optics were taken as a good reference for large dynamic aperture and high beam lifetime. Main operations parameters are, therefore, conserved off-energy (SR betatron tunes, optics at injection, photon sources, and collimators). This also eases the comparison between the two rings in a first approach. The ESRF-EBS global linear optics parameters to be conserved for the off-energy optics matching are: (i) the betatron tunes, (ii) the $-I$ transformation between symmetric sextupoles, (iii) Twiss functions and dispersion in the middle of the straight section and at the sextupoles (see Fig. 1), (iv) high β_x at the injection point for off-axis injection, and (v) chromaticity larger than (6,6) for beam stability at high bunch current.

The SR optics must also include: three canted straight sections and eight short bend (SB) and three short wiggler (SW) photon sources present in the ESRF-EBS SR. This section will describe in more detail the necessary optics matching steps to produce an off-energy lattice for the ESRF-EBS storage ring, starting from its standard cell.

A. Off-energy standard cell

To match the standard cell of the on-energy ESRF-EBS optics, nine quadrupole families were used to fix nine optics constraints: each constraint acts almost independently on specific cell parameters, such as detuning with

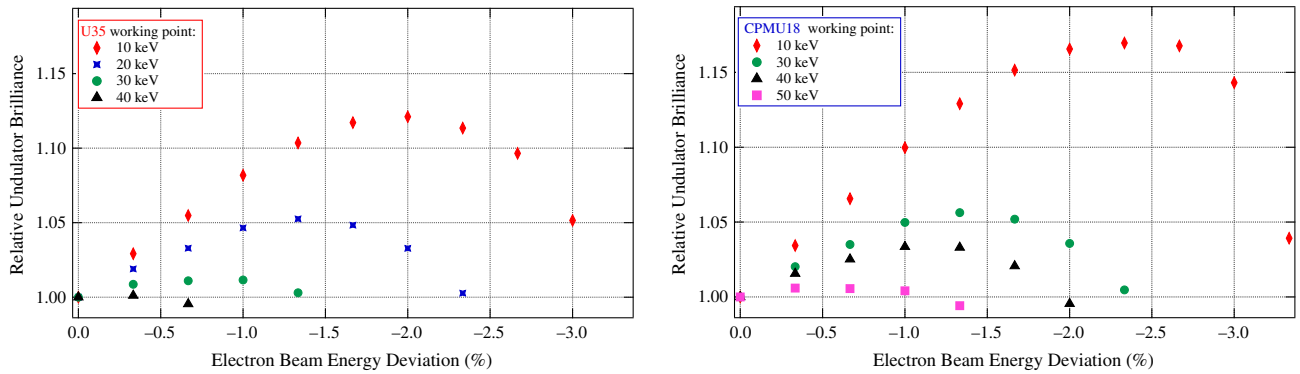

FIG. 4. Estimated maximum brilliance relative to nominal for two typical ESRF-EBS in-air (U35) and in-vacuum (CPMU18) undulators at different photon energies (markers), for different storage ring energy detuning. Each change in energy required an optics matching (see Appendix A). For sake of comparison and simplicity, the generated rings are 32-fold periodic.

amplitude and phase space at injection [3,32]. The matching of the off-energy cell may in principle use the same strategy. The Twiss functions and the dispersion of the off-energy optics were matched within the arbitrary ±5% range around the nominal Twiss parameters to ease the matching conditions and focus on restoring the betatron tunes and the $-I$ transformation as well as the β-functions at the center of the straight section.

The control of the cell phase advance requires the extensive use of the DQ magnets. To cope with their limited tuning range (±1%), their strengths were fixed to −0.49% of their nominal value. Additionally, the off-energy reference closed orbit also goes off axis in the sextupoles located under large dispersion bumps; this generates a parasitic quadrupolar component expressed as

$$k_1^{\text{sext}} = 2k_2 D_x \delta, \tag{2}$$

with k_2 the sextupole strength and D_x the dispersion at the sextupole. Consequently, any chromaticity correction leads to an undesired tune variation and dispersion deviation along the lattice. This quadrupolar component in the sextupoles can theoretically be compensated using the nearby quadrupoles to recover the tunes at the desired chromaticity. Nonetheless, this compensation affects the phase advance between the sextupoles thus jeopardises the $-I$ transformation. Therefore, the linear optics matching variables simultaneously included: the quadrupoles for linear optics and discreet compensation of the parasitic effect in Eq. (2) and the sextupoles for chromaticity. This parasitic effect could be avoided with a horizontal displacement of 600 − 800 μm of the sextupoles to place them onto the off-energy closed orbit. This option could not be tested for absence of motorized platforms on the sextupoles and lack of time for a realignment of the magnets.

Despite this discreet chromaticity correction, no magnet settings could conserve chromaticity larger than (6,6) for operation and the betatron tunes of the cell with the ESRF-EBS Twiss constraints. Therefore, the horizontal β-function in the middle of the straight section was increased from 6.90 to 7.25 m to accommodate both constraints. The horizontal beam size is enlarged by 2.5% which represents no limitation for our proof of principle. Figure 5 compares the Twiss functions and dispersion of the on- and off-energy optics. Table I extracts the main parameters and the electron beam sizes of two 32-fold periodic lattices composed of the on-energy standard cell and the off-energy matched optics. A reduction of 22 pm rad of the natural horizontal emittance is achieved as foreseen in Fig. 3. The second part of Table I compares the β-functions, dispersion, and electron horizontal beam sizes of the on- and off-energy optics at the center of the straight section. In all, the off-energy standard optics reduces the horizontal beam size by 7% and divergence by 11% at the insertion device. The strength variation of each magnet family compared to the on-energy optics is listed in Appendix B. All changes remain under the power supply limits.

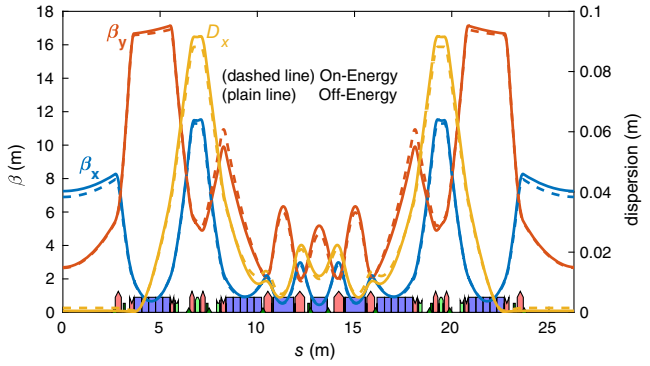

FIG. 5. Twiss functions of the standard cell of (plain) the off-energy and (dashed) the on-energy ESRF-EBS storage ring lattice.

B. High-β_x injection straight section

The high-β_x straight section for off-axis injection in the ESRF-EBS storage ring [33] was adapted to the off-energy optics. The two surrounding cells are identical to the standard ones, except the five quadrupole families adjacent to the injection point, required for optics matching. For sake of simplicity, the sextupoles in these two cells were left identical to the standard ones, leaving six knobs for later lifetime optimization.

Figure 6 compares the Twiss functions and dispersion of the on- and off-energy injection cells optics. The injection β_x for the off-energy optics is increased from 18.6 to 19.0 m maintaining a large dynamic aperture for off-axis injection. As for the on-energy optics, the introduction of the

TABLE I. Comparison of main optics matching parameters for two 32-fold symmetric on- and off-energy rings.

Parameter	On-energy	Off-energy
Energy (GeV)	6	5.94
Δf_{rf} (Hz)	0	280
(Q_x, Q_y)	(76.18, 27.34)	(76.18, 27.34)
(ξ_x, ξ_y)	(8.0, 5.4)	(6.8, 6.1)[a]
ϵ_x (pm rad)	133.1	111
α_C	8.53×10^{-5}	7.55×10^{-5}
σ_E	9.37×10^{-4}	1.0×10^{-3}
b_l ($I = 0$ mA) (mm)	3.07	2.97
Middle straight section		
(β_x, β_y) (m)	(6.90, 2.7)	(7.25, 2.7)
D_x (mm)	1.46	0.504
σ_x (μm)	30.3	28.3
σ'_x (μrad)	4.4	3.9

[a]The values of the chromaticity reported are the slope of the tune versus energy, at the energy set point, i.e., $\delta = -1\%$ in the off-energy case.

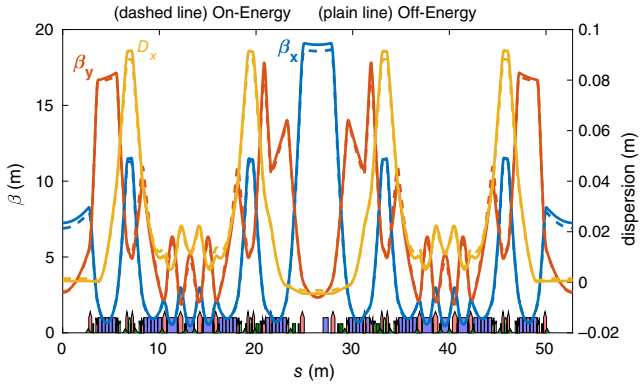

FIG. 6. Twiss functions of the injection cells of (plain) the off-energy and (dashed) the current ESRF-EBS storage ring lattice.

injection cell has a non-negligible impact on the ring performances. This degradation might be partially recovered by appropriate optimization of the injection cell sextupoles (see Sec. IV C).

C. Canted cells and local lattice modifications for SB and SW photon sources

Three straight sections are equipped with canting dipoles, allowing to direct x rays to two independent beamlines [34]; each has a peculiar canting angle. As for the injection cells, the first four quadrupoles neighboring the canted section are used for local optics matching. The modified dipole field distribution results in different dispersion and optics in these straight sections.

Seventeen photon sources exploit a large-band photon beam generated by a high-field short bend or a short wiggler, which are inserted close to the center of the cell. Such devices were included in the lattice, after insertion of the canted cells. Their effect on the Twiss functions and dispersion was compensated by the quadrupole families inside the $-I$ transformation. Despite the use of all available quadrupoles, the dispersion periodicity could not be fully restored, but the deviation does not generate impact on the lattice performances.

After insertion of all photon sources, the natural emittance of the off-energy lattice is 122 pm rad compared to the 141 pm rad for the on-energy lattice: a 13% reduction. Table II lists the main parameters of the 6 GeV ESRF-EBS HMBA lattice and its off-energy option, after inclusion of the high-β_x injection straight section and all canted straight sections and photon sources. The lower momentum compaction factor of the off-energy settings with corrected optics reduces the rf frequency shift required to set the energy deviation to -1% at 280 Hz, following Eq. (1).

D. Dynamic aperture and Touschek lifetime

Figure 7 compares the dynamic aperture at the injection point of the on- and off-energy perfect lattices and for both considered energy deviations, 0% and -1%. Particles were tracked for 10 000 turns, including radiation damping. The considerably reduced dynamic aperture of the on-energy optics at a -1% energy deviation was entirely recovered and even exceeded with the off-energy optics developed in the previous section, while presenting a 30% reduction in lifetime. This reduction is mainly due to the shifted

TABLE II. Main parameters of the ESRF-EBS storage ring lattice at its nominal energy and its off-energy version.

Parameter	On-energy	Off-energy
Energy (GeV)	6	5.94
Δf_{rf} (Hz)	0	280
(Q_x, Q_y)	(76.18, 27.34)	(76.18, 27.34)
(ξ_x, ξ_y)	(7.0, 6.0)	(6.6, 6.2)[a]
ϵ_x (pm rad)	141	122
α_c	8.62×10^{-5}	7.65×10^{-5}
σ_E	9.5×10^{-4}	1.0×10^{-3}
b_l ($I = 0$ mA) (mm)	2.98	3.02
U_0 (MeV)	2.6	2.5
β_x at injection (m)	18.5	19.0

[a]The values of the chromaticity reported are the slope of the tune versus energy, at the energy set point, i.e., $\delta = -1\%$ in the off-energy case.

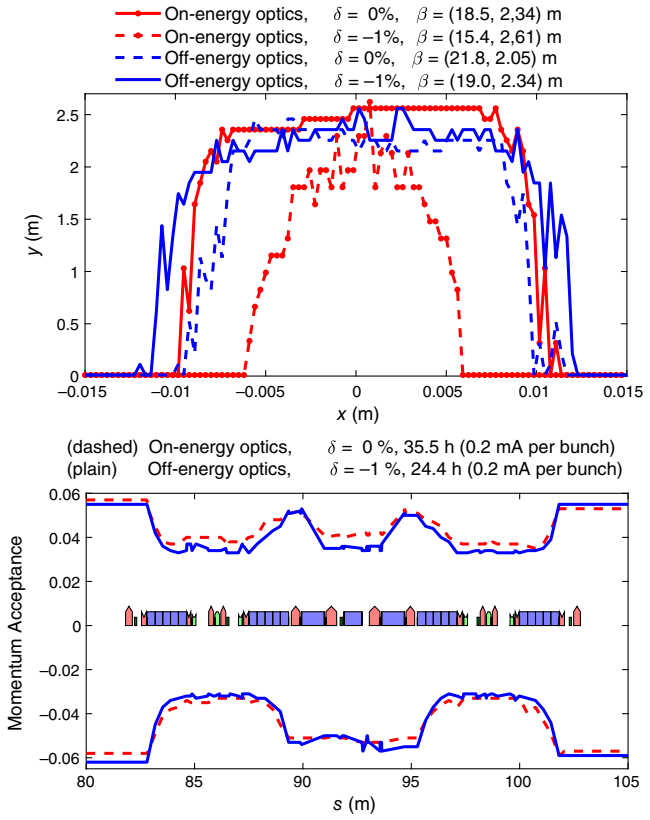

FIG. 7. Top: dynamic aperture and β-functions at the injection point for both energy deviation 0% and -1% and bottom: momentum acceptance over one standard cell and Touschek lifetime of the nominal lattice and its off-energy settings.

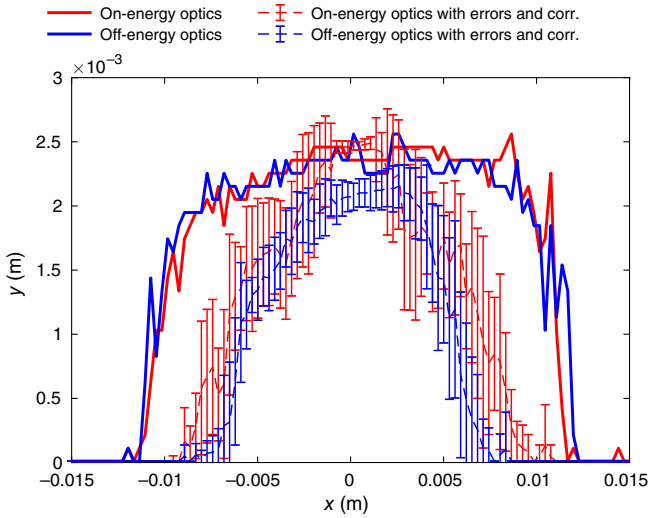

FIG. 8. Dynamic aperture at the injection point for the nominal lattice and its off-energy optics at their respective energy set point ($\delta = 0\%$ and $\delta = -1\%$), with and without errors and corrections.

momentum acceptance induced by the energy deviation working point.

To confirm these performances for operation, ten lattices including errors and correction were generated on-energy, including the alignment, gradient, and high-order multipole errors and tolerances listed in [35]. The quadrupole and sextupole strength differences between the on- and off-energy optics were then added to each generated lattice to produce their off-energy counterpart. This procedure transposes the corrections calculated and applied on-energy to the off-energy lattices with errors; it is a simplified commissioning-like simulation yet illustrates the implementation procedure of the off-energy settings in the SR and provides a lower estimate of the off-energy optics performances. These ten sets of errors and correction were then used either for on- or off-energy dynamic aperture and lifetime computations.

Figure 8 compares the dynamic aperture at the injection point of the perfect lattices to the averaged dynamic aperture of the lattices with errors and corrections, including standard deviation (error bars) for both optics under study. The dynamic aperture with errors and correction is reduced when switching to the off-energy optics. The reduction is, however, expected to be limited, approximately 1 mm, giving confidence for the setup and detailed correction process when testing with real beam (see Sec. IV). The lifetimes were calculated for three operation currents per bunch, displaying a 30% lifetime reduction from on- to off-energy at high current. The calculation parameters are available in Appendix C. The results are listed in Table III.

E. Brilliance, coherence, and beam sizes

The brilliance and coherent fraction of the final off-energy optics are compared to the on-energy lattice.

TABLE III. Touschek lifetime calculations (h) for three currents per bunch for on- and off-energy optics with the same ten sets of errors and corrections, assuming $Z_{//} = 0.52\ \Omega$ and $\epsilon_y = 10$ pm rad.

Current per bunch (mA)	On-energy	Off-energy
0.2, without errors	35.5	24.4
0.2	34.1 ± 1.1	26.8 ± 2.2
5.8	3.6 ± 0.1	2.59 ± 0.21
10	2.2 ± 0.1	1.78 ± 0.15

TABLE IV. Theoretical horizontal and vertical electron beam sizes $(\sigma_{x,y}, \sigma'_{x,y})$ at the photon sources for the on- and the off-energy lattices.

		Beam size and divergence	
Source	Plane	On-energy	Off-energy
ID	x	(31.2 μm, 4.52 μrad)	(29.7 μm, 4.10 μrad)
	y	(5.16 μm, 1.94 μrad)	(5.19 μm, 1.93 μrad)
BM	x	(23.7 μm, 25.0 μrad)	(25.2 μm, 25.4 μrad)
	y	(5.00 μm, 4.35 μrad)	(5.24 μm, 4.52 μrad)

Table IV lists the beam sizes at the location of insertion devices and bending magnet sources used for the brilliance and coherence calculations: a 5% reduction of the horizontal beam size and 10% in the divergence is achieved with the off-energy optics at the location of the insertion devices.

Figure 9 compares the brilliance of the emitted radiation from an in-air (U35) and an in-vacuum (CPMU18) undulators for the on-energy and the off-energy lattices. Calculations were conducted under the assumption that the radiation is emitted at the same photon energy. This required to open the undulator gap for the off-energy

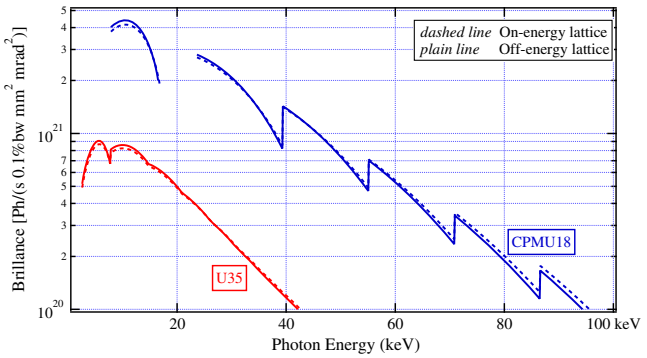

FIG. 9. Comparison of the brilliance for different photon energies for (plain) the off-energy and (dotted) the on-energy lattices for the case of an in-air (U35) and an in-vacuum (CPMU18) undulators. A maximum gain of 6% for the CPMU18 and 5% for the U35 is achieved for the fundamental harmonic.

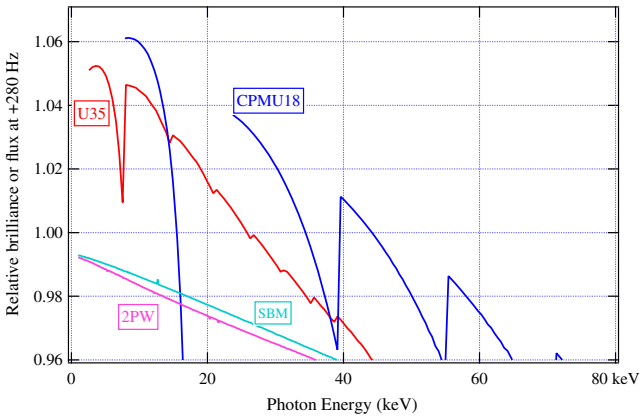

FIG. 10. Brilliance ratio of the off-energy versus on-energy settings for an in-air (U35) and an in-vacuum (CPMU18) undulators, an SB and an SW (2PW) photon sources.

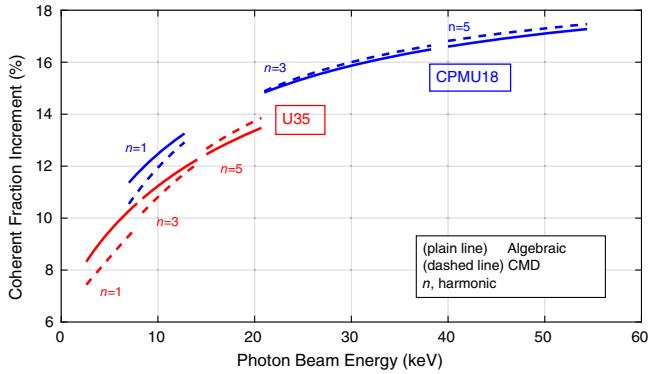

FIG. 11. Horizontal coherent fraction increment with photon energy, for the off-energy electron beam relative to the on-energy beam and for two photon sources: an in-air undulator (U35) and an in-vacuum undulator (CPMU18). Two calculation methods were used: the standard algebraic approximation and the CMD.

settings thus reducing the emitted photon flux and the resulting brilliance in that case. Figure 10 displays the ratio of the on-energy and off-energy brilliance curves, to ease the comparison.

The off-energy optics gain is focused on the fundamental and third harmonics as expected from Fig. 4, as higher orders suffer from the increased energy spread and consequent loss of flux. Nonetheless, the brilliance gain in the first two harmonics is lower than estimated in Fig. 4.

In order to preserve critical linear optics characteristics (cf., Sec. III) and maintain chromaticity larger than (6,6), the horizontal β-function in the straight section had to be slightly increased with respect to the on-energy lattice. Better performances could be achieved with undulators adapted to the off-energy settings, providing higher flux at the same photon energy.

The effect of the off-energy optics on the coherent fraction was calculated using the standard approximation of the ratio between the photon beam sizes emitted by a single electron versus an electron beam (algebraic method) [36] and by coherent mode decomposition (CMD) [37] for the first, third, and fifth harmonics of an in-air (U35) and an in-vacuum (CPMU18) undulators, at the source point. Details on the simulations are provided in Appendix D. Figure 11 shows the relative variation of the coherent fraction for different photon energies for the off-energy electron beam compared to the on-energy. There is a minimum increment of 10% for the CPMU18 harmonics and 9.0% in the case of U35.

Table V gathers the averaged increments for the three first harmonics of both photon sources. This could be appealing for beamlines that use coherence exploiting techniques such as ptychography or phase-contrast imaging. Energy dispersion has not been taken into account in the simulations. Per [38], the off-energy energy spread was considered sufficiently small not to affect the coherent fraction in our case.

Given these realistic estimations with the matched off-energy optics, the gain in brilliance is at most 6% for the fundamental harmonic of an in-vacuum undulator (CPMU18) and 5% for an in-air undulator (U35) instead of the estimated 8–10% from Fig. 3. In both cases, the coherent fraction is increased by at least 9–10% in both cases. In case of interest of such performances from the beamlines, experiments will be planned to confirm these values and will make object of a separate dedicated study.

IV. EXPERIMENTAL VALIDATION OF THE OFF-ENERGY OPTICS

The off-energy settings were tested on the ESRF-EBS storage ring at low and nominal currents, with an uniform and 7/8 filling patterns. For a fair comparison, the nonlinear optimization of the sextupoles and octupoles were removed from the on-energy lattice: this reference lattice will be referred to as the on-energy or periodic option in the following sections. To minimize the risk of beam losses while shifting the rf frequency and to set the optics, the following procedure was observed at 5 mA beam current (below the beam position interlock threshold): (i) fraction a of the total $\Delta f_{\mathrm{rf}} = 280$ Hz, (ii) tunes and orbit correction, (iii) fraction a of Δk_{quad} added on the quadrupole correction

TABLE V. Averaged increment (%) and standard deviation of the coherent fraction calculated for the off-energy and on-energy beams at the source point, for three harmonics (n) of two photon sources and the two calculation methods.

	CPMU18		U35	
Harmonics	Alg.	CMD	Alg.	CMD
$n = 1$	12.4 ± 0.6	11.8 ± 0.7	9.5 ± 0.7	8.6 ± 0.7
$n = 3$	15.8 ± 0.5	15.9 ± 0.5	11.5 ± 0.5	11.2 ± 0.6
$n = 5$	17.0 ± 0.2	17.2 ± 0.2	13.0 ± 0.3	13.3 ± 0.4

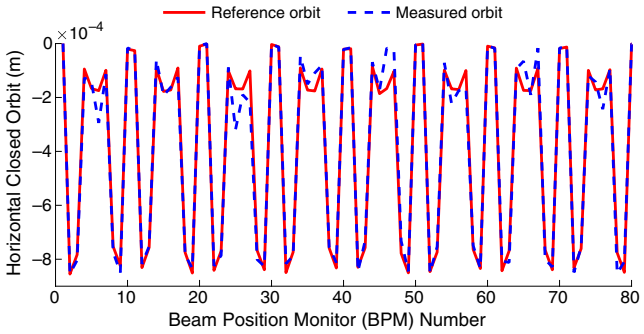

FIG. 12. Closed orbit measurement in a quarter of the ESRF-EBS SR for the off-energy settings. The red plain line corresponds to the reference orbit, the blue dashed line to the measured orbit at the beam position monitors (BPM) in the horizontal plane.

strengths after tune correction, and (iv) fraction a of Δk_{sext} added on the sextupole correction strengths.

The Δk_{quad} and Δk_{sext} are the strength differences between the off-energy and on-energy theoretical lattices. The correction of the tunes was conducted with the operational 2×2 response matrix, omitting the effect on the chromaticity and on the optics peculiar to the off-energy optics (cf., Sec. III A). The orbit correction response matrices are very similar since the off-energy optics are comparable to the on-energy ones (within 5%). In fact, the on-energy orbit response matrix allowed to correct the orbit off-energy. Figure 12 compares the measured closed orbit of the off-energy settings to the reference orbit corresponding to a 280 Hz rf frequency shift after the application of the above procedure.

A. Linear optics measurements

Characterization of linear optics was conducted thanks to an ESRF operation MATLAB application [39], on the on- and off-energy settings before and after correction and for the two relevant energy shifts. The β-functions and the dispersion are compared with their respective theoretical model. The standard deviations from theory are listed in Table VI.

Comparable beta-beating and dispersion deviation are measured for the on- and off-energy at their respective beam energy, both before and after correction within measurement errors [40]. The evaluation before correction corroborates the protocol in Sec. III D, and the assumption that the errors and correction implemented on-energy can be transferred to the off-energy lattice. The measurement of the on-energy optics at 280 Hz was for the sake of comparison, applying the rf shift on top of the corrected on-energy optics. After correction, the on- and off-energy settings present comparable beta-beating below 1% and dispersion deviation below 0.5 mm. The vertical beta-beating after correction for the off-energy optics is larger than the on-energy one: further optics correction iterations could improve this result. The nominal chromaticities were measured at $(10, 10) \pm (1, 1)$ for the on-energy optics, which corresponds to the operation values, and $(8.4, 9.3) \pm (1, 1)$ for the off-energy optics. This value is considered high enough to ensure beam stability in high bunch current modes [5]. The relative change between the measured chromaticities is in agreement, within the measurement error range, with the simulated difference in Table II.

TABLE VI. Beta-beating and dispersion deviation measurements for five experimented cases.

Parameter	On-energy		Off-energy		
Correction	False	True	False	False	True
rf shift	0 Hz	0 Hz	280 Hz	280 Hz	280 Hz
$(\frac{\Delta\beta}{\beta})_x \pm 1\%$	1.4%	0.42%	3.2%	1.7%	0.52%
$(\frac{\Delta\beta}{\beta})_y \pm 1\%$	1.6%	0.56%	0.57%	2.6%	0.96%
$\Delta D_x \pm 10\,\mu\mathrm{m}$	0.89 mm	0.40 mm	5.63 mm	1.62 mm	0.42 mm

B. Dynamic aperture measurement

The horizontal dynamic aperture boundaries were measured moving one of the two available collimators [41] while monitoring the total particle losses and beam lifetime. The measured dynamic aperture is defined as the position of the collimator where the lifetime of a horizontally blown-up beam filling the full dynamic aperture starts to drop [42]. One measurement is reported in Fig. 13 along with the fitting analysis.

Table VII extracts the obtained results scaled to the injection point. The contribution of the dispersive orbit at the collimator is also taken into account. As expected from simulations in Sec. III D, the off-energy optics allow to operate with a similar DA to the on-energy one [43].

The lower storage ring energy requires a scaling of the injected beam energy (tuned by the extraction time), the

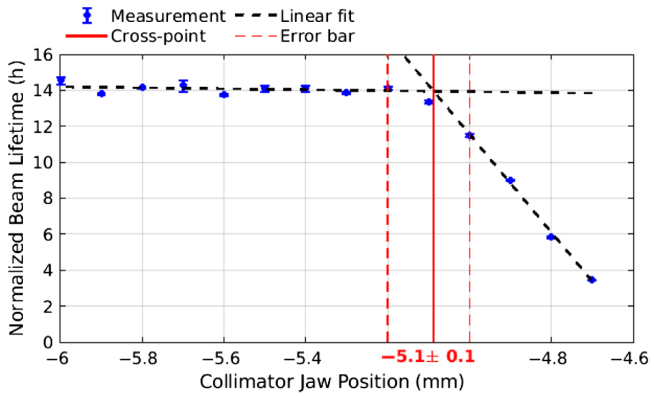

FIG. 13. Normalized beam lifetime with current versus the position of the inner collimator jaw in cell 24. The black lines fit the measurements, and the red lines extract the stability limit and its experimental error.

TABLE VII. Measured positive and negative horizontal dynamic apertures scaled to the injection point of the periodic on-energy and off-energy lattices without sextupole and octupole tuning.

Optics	rf shift (Hz)	Horizontal DA (mm)
On-energy	0	$[-6.5 \pm 0.2 : 6.0 \pm 0.2]$
	280	$[-5.4 \pm 0.2 : 4.9 \pm 0.3]$
Off-energy	0	$[-5.0 \pm 0.2 : 4.3 \pm 0.2]$
	280	$[-6.3 \pm 0.2 : 6.0 \pm 0.4]$

septum magnets, and the extraction transfer line magnets. At the time of the optimization, control issues with the booster extraction bumpers prevented any modification of the extraction time. Therefore, and due to the limited available experimental time, the injection efficiency (IE) was only tuned with the two extraction septa during the ramping up in current in the off-energy settings. The injection efficiency was maximized to 65% for a reduction of 0.5%–1% of the septa currents, which was comparable to the 60%–70% IE of the on-energy optics at the time of the MDT.

C. Touschek lifetime optimization

Lifetime optimization is carried out at every restart of the storage ring to ensure the best performances for the coming USM run. A total of twenty-four sextupole and four octupole knobs are tuned in sequence to minimize the total losses along the ring, at high current (200 mA) and at a fixed vertical emittance (typically 10 pm rad) [44].

In order to optimize the off-energy optics at high current, the efficiency of the vacuum chambers x rays distributed absorption is assessed for the off-energy optics. Considering the off-energy closed orbit displayed in Fig. 12, the trajectory of the parasitic radiation emitted by the combined-functions dipoles and high-gradient quadrupoles hits the absorber with a +1 mm external horizontal position than the on-energy photon beam. The remaining protective distance on the absorber thus reduces from ±3 to ±2 mm, considering an uncertainty on the position of the absorber of ±1 mm. This margin is large enough to protect the vacuum chamber from synchrotron radiation at high total current, including errors on the source position and angle, following the same requirements defined for the EBS lattice [4,6], allowing high total beam current experiments with the off-energy settings in the EBS storage ring.

The off-energy optics were tested at high current (200 mA) to measure and compare the beam lifetime to that expected in simulations (see Table III). The orbit distortion measured and displayed in Fig. 12 triggers the beam protection interlock (BPI), as it exceeds 1 mm in some beam position monitors (BPMs). The experiments at high current required to bypass the BPI threshold by integrating a reading offset in the triggered BPMs corresponding to the off-energy reference trajectory. The vacuum pressure was monitored while ramping the electron beam current to ensure the off-axis beam would not cause any outgassing.

TABLE VIII. Measurements of the Touschek and vacuum lifetimes (%) of the on-energy and off-energy lattices at $\epsilon_y = 10$ pm rad, before (without sextupole and octupole tuning) and after lifetime (h) optimization.

	Before optimization		After optimization[a]	
Optics	On-energy	Off-energy	On-energy	Off-energy
Vacuum	86 ± 22	65 ± 20	114 ± 25	126 ± 26
Touschek	26 ± 7	13 ± 6	33 ± 7	28 ± 6

[a]These values include a maximum 10% lifetime gain due to polarization during the optimization.

Table VIII compares the measured vacuum lifetime and the measured Touschek lifetime of the 200 mA uniform electron beam for different optic settings, gaps opened and collimators closed to the operation settings and a vertical emittance of 10 pm rad. The on-energy lifetimes before and after optimization were measured during the latest restart of the SR, following the standard procedure on periodic optics.

A quick optimization was conducted for the off-energy settings, using ten (instead of the standard twenty-four) sextupole and four octupole knobs, described in [44]. Figure 14 compares total lifetime measurements versus the vertical emittance from which are extracted the vacuum and Touschek lifetimes, of the on-energy operation lattice and the off-energy optics after optimization. The sextupole settings determined offline lead to beam lifetimes (normalized to 10 pm rad, 200 mA) of 13 h, almost a factor 2 less than the expected from simulations (cf., Table III). Nevertheless, online optimization of these settings could restore comparable values to the ones expected from simulations (cf., Table III) without affecting operation efficiency.

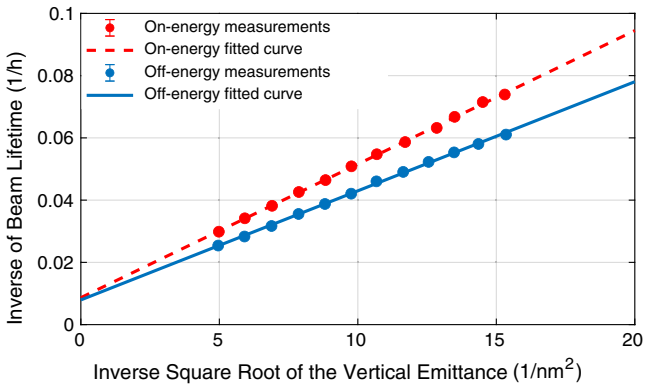

FIG. 14. Measurement of the vacuum lifetime and the Touschek lifetime after optimization of the (blue) off-energy optics and (red) the on-energy optics.

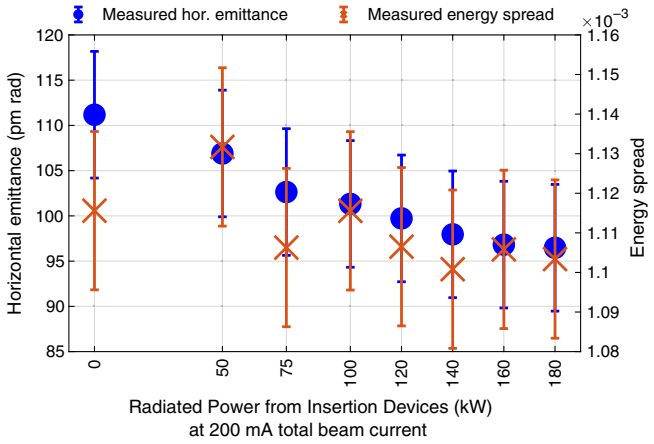

FIG. 15. Measured horizontal emittance and energy spread with progressively closed insertion device gaps and their expected radiated power at high total current (200 mA), for the off-energy settings of the ESRF-EBS storage ring. The emittance measurement was corrected according to the off-energy β-functions and dispersion at the pinhole in cell 07.

D. User mode simulation

To simulate the user mode, radiation power was generated in the machine by evenly closing the gaps of the insertion devices at low current (approximately 5 mA). Figure 15 gathers the measured horizontal emittance for different expected radiated powers at high total current (200 mA), with no vertical beam blowup (flat beam).

During user time, the emitted power typically varies within 80–120 kW at 200 mA total beam current. At this power, the measured equilibrium horizontal emittance with no vertical beam blowup is approximately 100 pm rad (about 120–130 pm rad for the on-energy case during user service mode).

V. CONCLUSIONS AND PERSPECTIVES

Off-energy optics were successfully developed for the ESRF-EBS storage ring, demonstrating a reduction of its horizontal emittance from 140 to 121 pm rad for an energy offset of -1%: this theoretical 20 pm rad reduction was successfully demonstrated in the ESRF-EBS storage with gaps opened. The simulated maximum brilliance gain in these settings reaches 6% for the fundamental harmonic of an in-vacuum ID (CPMU18) and 5% for an in-air ID (U35), at the same wavelength. For both typical ESRF undulator cases, the coherent fraction is on average increased by 13% for the CPMU18 and 9% for the U35 within the fundamental harmonic. Higher brilliance could be expected with more margin on the horizontal displacement of the DQ magnets or a complete realignment of the electromagnetic dipoles.

The off-energy optics were matched to remain as close as possible to the operation optics: all quadrupoles and sextupoles were varied to restore the HMBA characteristics and operation parameters, within the EBS power supply limits. This optics choice provided similar simulated dynamic aperture at injection and high enough beam lifetime for operation. Better performances could be obtained with different betatron tunes and Twiss functions in the off-energy settings, limiting the effect of the parasitic quadrupolar field of the sextupole on the linear optics or by realigning the sextupoles onto the off-energy closed orbit (600–800 μm displacement).

Another option radially translates all the magnets (DQs and high-gradient quadrupoles) located in the cell center away from the center of the SR. The induced orbit distortion is thus limited to the central part of the cell, with minimum impact on the linear optics. Similarly, reverse bending magnets could be included in the cell center to further reduce the horizontal emittance, at the detriment of the dynamic aperture and beam lifetime. Both techniques allow reduction of the beam emittance to about 100 pm rad without reduction in the beam energy, thus conserving the EBS flux. These options could not be tested on the ESRF-EBS SR.

The experiments conducted during machine dedicated time on the ESRF-EBS storage ring confirmed these results. The off-energy optics implementation was successful and straightforward. The measured horizontal emittance was 111 ± 7 pm rad in the ESRF-EBS storage ring, with gaps opened, confirming the 20 pm rad theoretical reduction (within the measurement error range). Moreover, all operational optics tuning tools (tune, orbit, optics, and coupling) operated without modification for the off-energy settings. The operability of the off-energy settings in the ESRF-EBS is limited by the impact of the large closed orbit distortion in the center of the cells induced by the rf frequency shift on the electron beam position and angle at the location of all the bending magnet sources. The beam arrives with an expected horizontal angle of 180 μrad, which would require an adjustment of around 4.5 mm at the end of the front end (FE). This is coupled with an increase of the electron beam sizes at the BMs, reducing the overall brilliance for these beamlines (see Appendix E).

In closing, off-energy operation improved the quality of the photon beam emitted from in-air and in-vacuum undulators in terms of brilliance and coherence while conserving the present EBS lattice design properties and operation performances. The off-energy principle may apply to a variety of storage ring light sources. Implementation of the off-energy optics as an operation mode would deliver higher brilliance x-ray beam for lower harmonics users at the detriment of higher harmonics users and a more coherent photon beam. This principle could also be applied in reverse for commissioning of future fourth generation storage rings starting with higher energy beam optics progressing toward the final design state in stages.

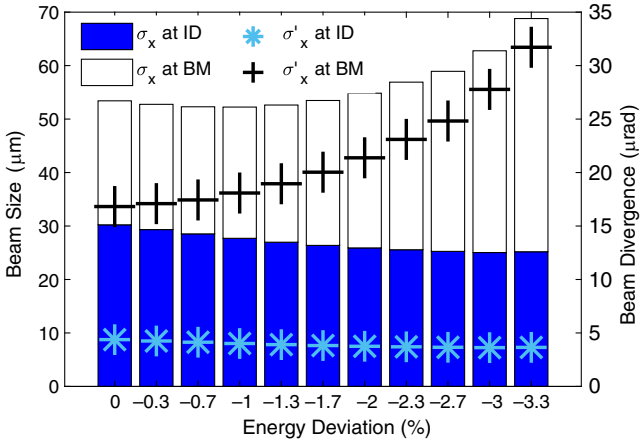

FIG. 16. Evolution of the horizontal beam sizes (bar) and divergences (marker) at the location of the ID sources (blue) and the BM sources (black).

ACKNOWLEDGMENTS

Many thanks to Manuel Sanchez del Rio for all the discussion and feedback on the CMD-WOFRY code and to the ESRF-EBS operators for their support during the experimental studies.

APPENDIX A: PERIODIC HMBA LATTICES FOR OFF-ENERGY BRILLIANCE ESTIMATIONS

For a finer estimation of the emittance reduction and brilliance gain, eleven 32-fold periodic lattices were generated for different energy deviations, up to −3.3%. Each lattice optics were rematched to approach the ESRF-EBS HMBA standard cell, conserving the betatron tunes of the ring, the $-I$ transformation between sextupoles, the β-functions at the middle of the ID, and a dispersion level below 1.5 mm at the ID. The optics correction exploited all quadrupole and sextupole families and disregarded any concerns regarding the feasibility of the generated standard cells in terms of power supply limits, beam lifetime, momentum, and transverse apertures. In particular, no control was set on the damping partition numbers nor the chromaticity. Specifically, for energy deviations lower than −1.3%, no magnet settings could simultaneously verify the sextupole phase advance constraints and maintain chromaticities higher than (6,6) for operation.

The main characteristics of the generated lattices in view of brilliance calculations are displayed in Table IX. The variation of the beam sizes at the location of the undulator sources and bending magnet sources are plotted with regards to the energy deviation in Fig. 16. While the beam sizes and divergence at the location of the IDs are decreased thanks to the reduction in both the emittance and the dispersion, despite the higher energy spread, the conservation of the aforementioned EBS HMBA key optics parameters results in the increase of the β-functions and dispersion at the location of the bending magnet sources.

APPENDIX B: MAGNET VARIATIONS FROM THE ON-ENERGY TO THE OFF-ENERGY LATTICE WITH OPTICS CORRECTION

Table X lists the relative variation with regard to the nominal settings of all magnet families used in the off-energy optics matching of the standard HMBA cell and the high-β_x injection cells. Similar values apply for the canted cells and cells modified for the installation of SB and SW photon sources. All magnet variations remain within their power supply limits.

TABLE IX. Parameters of the generated 32-fold periodic rings for an estimation of the brilliance gain in different applied rf frequency shifts, with $(\beta_x, \beta_y) = (6.90, 2.66)$ m at the location of the insertion devices.

ΔE (%)		0	−0.33	−0.67	−1	−1.3	−1.7	−2	−2.3	−2.7	−3	−3.3
ϵ_x (pm rad)		132	125	118	111	105	99.7	95.3	91.5	87.7	84.0	91.9
α_C (10^{-5})		8.5	8.3	8.0	7.7	7.3	7.0	6.6	6.2	5.9	5.5	5.0
σ_E (10^{-3})		0.94	0.96	0.99	1.0	1.1	1.1	1.2	1.3	1.4	1.6	1.6
ID	D_x (mm)	1.5	0.83	0.14	0.0015	6.9×10^{-5}	9.2×10^{-5}	7.4×10^{-5}	0.0023	0.020	0.010	-4×10^{-6}
	σ_x (μm)	30.2	29.3	28.5	27.7	26.9	26.2	25.6	25.1	24.6	24.1	25.2
	$\sigma_{x'}$ (μrad)	4.4	4.3	4.1	4.0	3.9	3.8	3.7	3.6	3.6	3.5	3.65
BM	β_x (m)	1.88	1.89	1.90	1.90	1.91	1.92	1.93	1.93	1.95	1.96	1.96
	β_y (m)	2.50	2.42	2.35	2.33	2.32	2.33	2.35	2.38	2.47	2.53	2.64
	D_x (mm)	18.2	18.5	18.7	19.4	19.4	21.1	22.0	23.0	23.6	24.7	26.1
	D'_x (mrad)	15.7	15.8	15.9	16.2	16.2	16.9	17.0	18.0	18.3	18.9	19.5
	σ_x (μm)	23.2	23.4	23.8	24.6	25.7	27.2	29.0	32.0	35.2	41.3	43.6
	$\sigma_{x'}$ (μrad)	16.8	17.1	17.4	18.1	19.0	20.2	21.6	23.7	26.0	30.7	31.7

TABLE X. Standard cell magnet relative variations used for the implementation of the optics correction at the off-energy settings.

Standard cell					
DQ	−0.49%	QF1	−1.7%	QD2	−1.7%
QD3	4.6%	QD5	−2.4%	QF4[AE]	0.23%
QF4[BD]	2.0%	QF6	−1.7%	QF8	−0.28%
SF	−4.0%	SD1[AE]	0.098%	SD1[BD]	−1.6%
Injection cells					
QD2[IJ]	−2.3%	QD3[IJ]	2.3%	QF4[IJ]	0.030%
QF1[IJ]	−1.5%	QF2[IJ]	−1.2%		

APPENDIX C: LIFETIME CALCULATION PARAMETERS

Table XI lists the parameters used to compute the estimations of the beam lifetime for the on-energy and off-energy cases (cf., Sec. III D). The momentum acceptance was tracked over the full rings. The tracking was done with A.T., including radiation damping.

APPENDIX D: COHERENCE CALCULATION PARAMETERS

Two sources were used for this study, a 2.5 m long undulator with 138 periods of 18 mm (similar to CPMU18 developed for some ESRF beamlines) and a typical ESRF 1.6 m long U35, with 46 periods of 35 mm. Simulations were performed for the first, third, and fifth harmonics of each undulator spectrum, and the coherent fraction was calculated directly at the source point, for faster and reliable simulations. As an example, simulations results for a 7 keV photon beam are shown in Fig. 17 comparing the occupied coherence of the first coherent mode, as defined in [37] for both electron beams and in the case of the CPMU18 undulator.

TABLE XI. Parameters for the calculations of the beam lifetime of the on-energy and off-energy lattices. The momentum acceptance was tracked over the full rings.

Parameter	On-energy	Off-energy
Number of turns	2000	2000
Energy deviation (%)	0	−1
Horizontal emittance (pm rad)	140	122
Vertical emittance (pm rad)	10	10
Energy spread	9.5×10^{-4}	1.0×10^{-3}
Current per bunch (mA)	(0.2/868, 0.092/16, 0.04/4)	
Bunch length (mm)	(4.5, 10.6, 12.6)	(4.4, 10.5, 12.6)
Effective impedance Z_n (Ω)	0.52	0.52

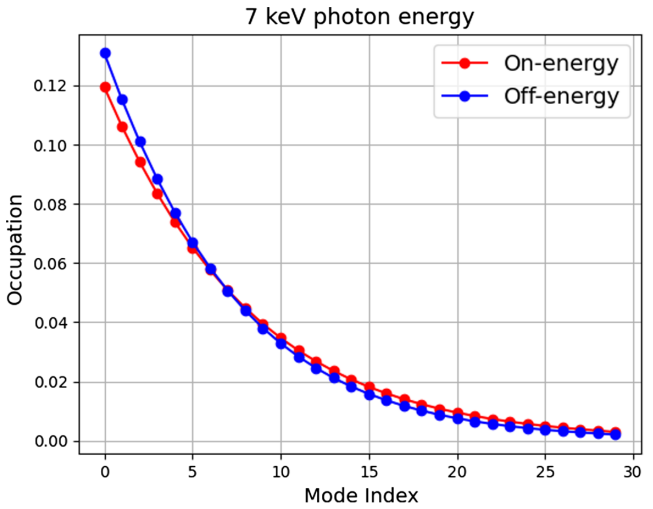

FIG. 17. Horizontal coherent occupation for each coherent mode for both electron beam parameters.

APPENDIX E: IMPACT OF THE OFF-ENERGY OPERATION ON THE BENDING MAGNET SOURCES

The off-energy optics are not transparent to the bending magnet sources. From Table IV, the electron beam sizes are increased at the entrance of such photon sources with the off-energy optics. Consequently, a reduction in the spectrum brilliance is observed, which should remain acceptable to the BM users. Figure 18 compares the simulated maximum brilliance of the spectrum emitted by an SB and an SW for the on- and off-energy lattices.

The large orbit distortion in the cell center created by the rf frequency shift displaces the electron beam position and angle at the entrance of all bending magnet sources. The horizontal angle of −180 μrad results in a horizontal translation of the photon beam at the front end (FE) of 4.2 mm at its last element. Table XII computes the expected aperture margin, assuming the off-energy photon

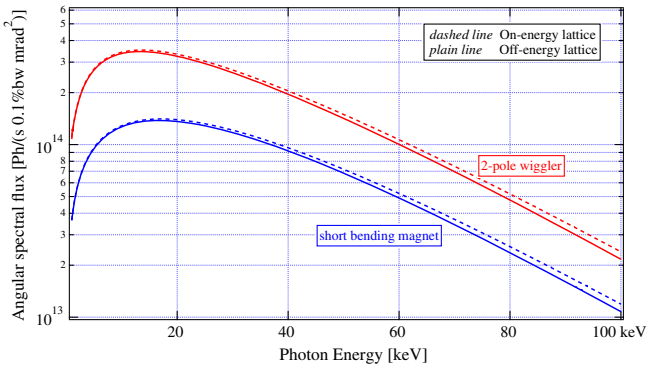

FIG. 18. Comparison of the angular spectral flux for different photon energies for the on-energy (dotted lines) and the off-energy lattices (plain lines) for the case of an SB and an SW.

TABLE XII. Aperture margin based on the off-energy photon beam size assuming the beam is centered on the mask and off-energy displacement at the present location of the masks.

BM type	Aperture margin (mm)	Off-energy displacement (mm)
SBM	±5	−4.2
2PW	± −0.8	−4.2
3PW	±4.5	−4.2

beam is centered on the mask. Including the off-energy displacement, the off-energy photon beam should still be seen by the SB and 3PW beamlines, as they used the central part of the arriving photon beam. The case of the short wiggler depends on its type, its mask, and the beam harmonic they exploit.

[1] N. Martensson and M. Eriksson, The saga of MAX IV, the first multi-bend achromat synchrotron light source, Nucl. Instrum. Methods Phys. Res., Sect. A **907**, 97 (2018).

[2] L. Liu, N. Milas, A. H. C. Mukai, X. R. Resende, and F. H. de Sá, The Sirius project, J. Synchrotron Radiat. **21**, 904 (2014).

[3] P. Raimondi, N. Carmignani, L. R. Carver, J. Chavanne, L. Farvacque, G. Le Bec, D. Martin, S. M. Liuzzo, T. Perron, and S. White, Commissioning of the hybrid multibend achromat lattice at the European Synchrotron Radiation Facility, Phys. Rev. Accel. Beams **24**, 110701 (2021).

[4] P. Raimondi, C. Benabderrahmane, P. Berkvens, J. C. Biasci, P. Borowiec, J.-F. Bouteille, T. Brochard, N. B. Brookes, N. Carmignani, L. R. Carver *et al.*, The Extremely Brilliant Source storage ring of the European Synchrotron Radiation Facility, Commun. Phys. **6**, 82 (2023).

[5] L. R. Carver, T. Brochard, E. Buratin, N. Carmignani, F. Ewald, L. Hoummi, S. M. Liuzzo, T. Perron, B. Roche, and S. White, Beam based characterization of the European Synchrotron Radiation Facility Extremely Brilliant Source short range wakefield model, Phys. Rev. Accel. Beams **26**, 044402 (2023).

[6] L. Farvaque, N. Carmignani, J. Chavanne, A. Franchi, G. Le Bec, S. M. Liuzzo, B. Nash, T. Perron, and P. Raimondi, A low-emittance lattice for the E.S.R.F., in *Proceedings of the 4th International Particle Accelerator Conference, IPAC2013, Shanghai, China* (JACoW, Geneva, Switzerland, 2013), p. 79, accelconf.web.cern.ch/ipac2013/papers/mopea008.pdf.

[7] K. L. Brown, First- and second-order matrix theory for the design of beam transport systems and charged particle spectrometers, Adv. Part. Phys. **1**, 71 (1968).

[8] R. V. Servranckx and K. L. Brown, Chromatic correction for large storage rings, IEEE Trans. Nucl. Sci. **26**, 3598 (1979).

[9] H. Wiedemann, *Particle Accelerator Physics*, 4th ed. (Springer Cham, 2015), 10.1007/978-3-319-18317-6.

[10] H. Onuki and P. Elleaume, *Undulators, Wigglers and Their Applications*, 1st ed. (CRC Press, Boca Raton, FL, 2002).

[11] S. White, G. Le Bec, and S. Liuzzo, Mini-beta optics for the European Synchrotron Radiation Facility, in *Proceedings of the 14th International Particle Accelerator Conference, IPAC2023, Venice, Italy* (JACoW, Geneva, Switzerland, 2023), p. 3130, 10.18429/jacow-ipac2023-wepl029.

[12] O. Manzhura, S. Bielawski, E. Bründermann, M. Caselle, S. A. Chilingaryan, T. Dritschler, S. Funkner, A. Kopmann, A-S. Müller, M. J. Nasse *et al.*, Terahertz sampling rates with photonic time-stretch for electron beam diagnostics, in *Proceedings of the 13th International Particle Accelerator Conference, IPAC2022, Bangkok, Thailand* (JACoW, Geneva, Switzerland, 2022), p. 263, 10.18429/JACoW-IPAC2022-MOPOPT017.

[13] A. Wolski, *Introduction to Beam Dynamics in High-Energy Electron Storage Rings* (Morgan & Claypool Publishers, 2018), pp. 3–1 to 3–24, 10.1088/978-1-6817-4989-1.

[14] A. Streun, The anti-bend cell for ultralow emittance storage ring lattices, Nucl. Instrum. Methods Phys. Res., Sect. A **737**, 148 (2014).

[15] B. Riemann and A. Streun, Low emittance lattice design from first principles: Reverse bending and longitudinal gradient bends, Phys. Rev. Accel. Beams **22**, 021601 (2019).

[16] J. P. Delahaye and J. P. Potier, Reverse bending magnets in combined function lattice for the CLIC damping ring, in *Proceedings of the 1989 Particle Accelerator Conference, PAC 1989, Chicago, IL* (IEEE, New York, 1989), Vol. 3, pp. 1611–1613.

[17] H. Wiedemann, *Particle Accelerator Physics*, 4th ed. (Springer Cham, 2015), p. 250, 10.1007/978-3-319-18317-6.

[18] M. Lamont, Maximising energy and luminosity, in *Proceedings of the 10th Workshop of the LHC* (CERN, Geneva, Switzerland, 2000), pp. 269–272.

[19] G. Arduini, R. Assmann, R. Bailey, A. Butterworth, P. Collier, K. Cornelis, S. Fartoukh, M. Lamont, G. Morpurgo, G. Roy *et al.*, Electron-Positron Collisions at 209 GeV, in *Proceedings of the 2001 Particle Accelerator Conference, PAC 2001, Chicago, IL* (IEEE, Piscataway, NJ, 2001), Vol. 3, pp. 356–358, 10.1109/PAC.2001.987514.

[20] R. Assmann, LEP operation and performance with electron-positron collisions at 209 GEV, in *Proceedings of the 11th Workshop of the LHC* (CERN, Geneva, Switzerland, 2001), pp. 323–334.

[21] N. Carmignani, N. Benoist, J.-F. B. Bouteille, M. G. Di Vito, F. Ewald, L. Farvacque, A. Franchi, O. Goudard, J. M. Koch, S. Lagarde *et al.*, Operation improvements and emittance reduction of the ESRF booster, in *Proceedings of the 9th International Particle Accelerator Conference, IPAC2018*, Vancouver, BC Canada (JACoW, Geneva, Switzerland, 2018), p. 4077, 10.18429/JACoW-IPAC2018-THPMF017.

[22] N. Carmignani, L. R. Carver, S. M. Liuzzo, T. P. Perron, and S. White, Operation of the ESRF booster with the new EBS storage ring, in *Proceedings of the 12th International Particle Accelerator Conference, IPAC2021, Campinas, Brazil* (JACoW, Geneva, Switzerland, 2021), p. 221, 10.18429/JACoW-IPAC2021-MOPAB051.

[23] F. Lin, J. Bengtsson, W. Guo, S. Krinsky, Y. Li, and L. Yang, Low horizontal beta function in long straights of the NSLS-II lattice, in *Proceedings of the 24th Particle Accelerator Conference, PAC 2011, New York* (IEEE, New York, 2011).

[24] A. Streun, G. Ingold, A. Al-Adwan, P. Beaud, M. Boege, J. Johnson, A. Keller, T. Schilcher, V. Schlott, T. Schmidt *et al.*, Sub-picosecond X-ray source femto at SLS, in *Proceedings of the 10th European Particle Accelerator Conference, Edinburgh, Scotland, 2006* (EPS-AG, Edinburgh, Scotland, 2006), pp. 3427–3429.

[25] C. Steier, E. Forest, L. Nadolski, H. Nishimura, D. Robin, W. Wan, Y. Wu, and A. Zholents, Accelerator physics challenges of the fs-slicing upgrade at the ALS, in *Proceedings of the 20th Particle Accelerator Conference, PAC 2003, Portland, OR* (IEEE, New York, 2003), Vol. 1, pp. 397–399.

[26] B. Nash, N. Carmignani, L. Farvacque, S. M. Liuzzo, T. P. Perron, P. Raimondi, R. Versteegen, and S. M. White, New functionality for beam dynamics in accelerator toolbox (AT), in *Proceedings of the 6th International Particle Accelerator Conference, IPAC2015, Newport News, VA* (JACoW, Geneva, Switzerland, 2015), p. 113, 10.18429/JACoW-IPAC2015-MOPWA014.

[27] AT Collaboration, 2022, https://atcollab.github.io/at.

[28] S. Liuzzo, N. Carmignani, J. Chavanne, L. Farvacque, B. Nash, and P. Raimondi, Optics Adaptations for Bending Magnet Beam Lines at ESRF: Short Bend, 2-Pole Wiggler, 3-Pole Wiggler, in *Proceedings of the International Particle Accelerator Conference, IPAC2017, Copenhagen, Denmark* (JACoW, Geneva, Switzerland, 2017), p. 666, 10.18429/JACoW-IPAC2017-MOPIK062.

[29] O. Chubar and P. Elleaume, Accurate and efficient computation of synchrotron radiation in the near field region, in *Proceedings of the 6th European Particle Accelerator Conference, Stockholm, 1998* (IOP, London, 1998), p. 1177, https://cds.cern.ch/record/858849.

[30] R. P. Walker, Undulator radiation brightness and coherence near the diffraction limit, Phys. Rev. Accel. Beams **22**, 050704 (2019).

[31] G. Geloni, S. Serkez, R. Khubbutdinov, V. Kocharyan, and E. Saldin, Effects of energy spread on brightness and coherence of undulator sources, J. Synchrotron Radiat. **25**, 1335 (2018).

[32] S. M. White, N. Carmignani, L. R. Carver, J. Chavanne, L. Farvacque, L. Hardy, J. Jacob, G. Le Bec, S. M. Liuzzo, T. P. Perron *et al.*, Commissioning and restart of ESRF-EBS, in *Proceedings of the 12th International Particle Accelerator Conference, IPAC2021, Campinas, Brazil* (JACoW, Geneva, Switzerland, 2021), p. 1, 10.18429/JACoW-IPAC2021-MOXA01.

[33] S. White and T. Perron, Injection using a non-linear kicker at the ESRF, in *Proceedings of the 13th International Particle Accelerator Conference, IPAC2022, Bangkok, Thailand* (JACoW, Geneva, Switzerland, 2022), p. 2679, 10.18429/JACoW-IPAC2022-THPOPT040.

[34] S. Liuzzo, N. Carmignani, J. Chavanne, L. Farvacque, T. P. Perron, P. Raimondi, and S. M. White, ESRF-EBS lattice model with canted beamlines, in *Proceedings of the 9th International Particle Accelerator Conference, IPAC2018, Vancouver, BC Canada* (JACoW, Geneva, Switzerland, 2018), p. 4081, 10.18429/JACoW-IPAC2018-THPMF019.

[35] R. Dimper, H. Reichert, P. Raimondi, L. S. Ortiz, F. Sette, and J. Susini, *ESRF Orange Book* (The European Synchrotron, 2015), pp. 69–70.

[36] M. S. Sanchez del Rio, About the coherent fraction of synchrotron emission, arXiv:1801.07542.

[37] M. S. Sanchez del Rio, R. Celestre, J. Reyes-Herrera, P. Brumund, and M. Cammarata, A fast and lightweight tool for partially coherent beamline simulations in fourth-generation storage rings based on coherent mode decomposition, J. Synchrotron Radiat. **29**, 1354 (2022).

[38] R. Khubbutdinov, A. P. Menushenkov, and I. A. Vartanyants, Coherence properties of the high-energy fourth-generation X-ray synchrotron sources, J. Synchrotron Radiat. **26**, 1851 (2019).

[39] S. M. Liuzzo, N. Carmignani, L. R. Carver, L. Farvacque, L. Hoummi, T. P. Perron, B. Roche, B. Vedder, and S. M. White, FILO: A new application to correct optics in the ESRF-EBS storage ring, in *Proceedings of the 13th International Particle Accelerator Conference, IPAC2022, Bangkok, Thailand* (JACoW, Geneva, Switzerland, 2022), p. 1401, 10.18429/JACoW-IPAC2022-TUPOMS006.

[40] R. Tomás, M. Aiba, A. Franchi, and U. Iriso, Review of linear optics measurement and correction for charged particle accelerators, Phys. Rev. Accel. Beams **20**, 054801 (2017).

[41] R. Versteegen, P. Berkvens, N. Carmignani, L. Farvacque, S. M. Liuzzo, B. Nash, T. P. Perron, P. Raimondi, and S. M. White, Collimation scheme for the ESRF upgrade, in *Proceedings of the 6th International Particle Accelerator Conference, IPAC2015, Newport News, VA* (JACoW, Geneva, Switzerland, 2015), p. 1434, 10.18429/JACoW-IPAC2015-TUPWA017.

[42] N. Carmignani, L. R. Carver, L. Valle, S. M. Liuzzo, T. P. Perron, B. Roche, and S. M. White, in Dynamic aperture measurement with a shaker magnet at the European Synchrotron Radiation Facility Extremely Brilliant Source storage ring (to be published).

[43] S. M. Liuzzo, N. Carmignani, L. R. Carver, L. Hoummi, T. P. Perron, and S. M. White, A long booster option for the ESRF-EBS 6 GeV storage ring, in *Proceedings of the 13th International Particle Accelerator Conference, IPAC2022, Bangkok, Thailand* (JACoW, Geneva, Switzerland, 2022), p. 1405, 10.18429/JACoW-IPAC2022-TUPOMS007.

[44] N. Carmignani, L. R. Carver, L. Hoummi, S. M. Liuzzo, T. P. Perron, P. Raimondi, and S. M. White, Online optimization of the ESRF-EBS storage ring lifetime, in *Proceedings of the 13th International Particle Accelerator Conference, IPAC2022, Bangkok, Thailand* (JACoW, Geneva, Switzerland, 2022), p. 2552, 10.18429/JACoW-IPAC2022-THPOPT001.